Newtonian fluid meets an elastic solid: Coupling lattice Boltzmann and lattice-spring models

Gavin A. Buxton,[1] Rolf Verberg,[1] David Jasnow,[2] and Anna C. Balazs[1]
[1]*Chemical and Petroleum Engineering Department, University of Pittsburgh, Pittsburgh, Pennsylvania 15261, USA*
[2]*Department of Physics and Astronomy, University of Pittsburgh, Pittsburgh, Pennsylvania 15260, USA*
(Received 12 November 2004; published 26 May 2005)

We integrate the lattice Boltzmann model (LBM) and lattice spring model (LSM) to capture the coupling between a compliant bounding surface and the hydrodynamic response of an enclosed fluid. We focus on an elastic, spherical shell filled with a Newtonian fluid where no-slip boundary conditions induce the interaction. We calculate the "breathing mode" oscillations for this system and find good agreement with analytical solutions. Furthermore, we simulate the impact of the fluid-filled, elastic shell on a hard wall and on an adhesive surface. Understanding the dynamics of fluid-filled shells, especially near adhesive surfaces, can be particularly important in the design of microcapsules for pharmaceutical and other technological applications. Our studies reveal that the binding of these capsules to specific surfaces can be sensitive to the physical properties of both the outer shell and the enclosed fluid. The integrated LBM-LSM methodology opens up the possibility of accurately and efficiently capturing the dynamic coupling between fluid flow and a compliant bounding surface in a broad variety of systems.

DOI: 10.1103/PhysRevE.71.056707 PACS number(s): 02.70.−c, 46.15.−x, 47.11.+j

I. INTRODUCTION

There are many systems of scientific importance where both the hydrodynamic response of a fluid and the mechanical response of an adjacent structure are dynamically coupled. For example, in the biomechanics of either blood flow in the cardiovascular system, or air flow in the respiratory system, the compliant nature of the vessels can have a significant effect on the flow rate and wall shear stresses [1,2]. Such fluid-flow–boundary interactions are commonly referred to as simply "fluid-structure" interactions. These fluid-structure interactions must also be taken into account to optimize the design of aeroelastic aircraft wings, which may experience "flutter" [3], or large civil engineering structures, which may undergo wind-induced oscillations and experience aerodynamic instabilities [4]. Computational modeling of fluid-structure interactions is, therefore, of significant importance to a wide range of scientific disciplines.

Conventional numerical solutions to fluid-structure interaction problems generally involve the coupling of a finite element method for the structural analysis with either a finite difference, finite volume, or finite element method to simulate the fluid dynamics. While the solid and fluid subsystems can be solved simultaneously [5], typically, an approach is adopted that involves separate computer codes for the solid and fluid systems [1,6,7]. In this so-called "partitioned" approach, the governing equations of the fluid and solid phase are solved individually and sequentially. The two codes are then coupled through the boundary conditions at the solid-fluid interface. For example, the stress that acts on the wetted boundary from the fluid domain is passed as a load to the solid domain, with the resultant deformation of the boundary being returned to the fluid domain. This process is repeated until consistent results are obtained that satisfy the constraints of both the fluid and the solid domains. The velocity of the boundary can then be quasistatically obtained from the difference in the boundary locations between consecutive time steps. This method of coupling two separate codes is particularly popular as it allows one to choose the most efficient and applicable codes for both the fluid and solid domains separately, thereby taking advantage of a wide range of commercial packages that solve for either the structural mechanics or the fluid dynamics.

Recently, however, lattice-based simulation techniques have emerged as promising alternatives to more conventional numerical schemes [8,9]. Unlike conventional numerical schemes (meaning methods involving a direct discretization of the continuum equations), these lattice models simulate the underlying processes that give rise to the appropriate continuum behavior. In particular, the lattice Boltzmann model (LBM) incorporates the mesoscopic physics of fluid "particles" propagating and colliding on a simple lattice such that the averaged, long-wavelength properties of the system obey the desired Navier-Stokes equation [9]. In a similar fashion, the lattice spring model (LSM) is adopted from atomistic models of solid-state and molecular physics [10], and involves a network of interconnected "springs," which describe the interactions between neighboring units. The large scale behavior of the resultant system can be mapped onto continuum elasticity theory [11]. The LBM and LSM are, therefore, both mesoscopic models, whose local rules are guided by atomistic phenomena, but whose emergent behavior captures the continuum properties of the system.

In this study, we take advantage of these mesoscale approaches to formulate a new technique for modeling solid-fluid interactions by dynamically coupling the lattice Boltzmann and lattice spring methods. To validate the method, we simulate the behavior of a Newtonian fluid that is enclosed in an isotropic, elastic, spherical shell. As we detail in Sec. II, this approach allows for a *dynamic* interaction between moving elastic walls and the enclosed fluid. The moving walls exert a force on the fluid and, in turn, the confined fluid reacts back on the walls. The specific system we consider here is of particular relevance to microencapsulated fluids. Microcapsules, which consist of an agent enclosed in an elastic shell, are becoming increasingly important in the pharma-

ceutical, cosmetics, and food industries. For example, microcapsules containing anticancer drugs can be tailored to target tumor cells or lesions [12]. In such applications, the adhesion of microcapsules onto specific surfaces can be essential to their functionality [13]. Therefore, in the current study, as a demonstration of the approach, we investigate the dynamics of a fluid-filled elastic shell and, in particular, examine the collision of this deformable capsule with either a hard or an adhesive surface. We note that a recent study by O'Brien and Bean [14] uses a similar methodology to couple two-dimensional lattice Boltzmann and lattice spring models. However, in their study the "lattice Boltzmann" (or fluid) nodes and the "lattice spring" (or solid) nodes are part of one and the same lattice. They then obtain the "spring forces" on the links connecting fluid and solid nodes directly from the solid-fluid boundary condition, using the same bounce-back rule as used in our study [see Eq. (14) below]. This method, however, does not allow for large deformations of the solid-fluid interface.

Before discussing the different methods in detail, we provide a brief background of the LBM and LSM. In particular, the lattice Boltzmann method is an effective and expedient method for simulating fluid flows. It has been shown to be particularly effective for simulating the hydrodynamic behavior of complex, multiphase fluids and fluid flow around complicated boundaries. For example, it has been used to simulate the phase separation of binary [15–17], ternary [18], and reactive multiphase fluids [19]. Recently, a large number of deformable biological cells (separate fluid phases) were simulated in veinule flow [20]. The relative ease with which the LBM can be implemented at irregularly shaped boundaries has facilitated the modeling, for example, of (reactive) fluid flow through porous media [21–23] and blood flow through stationary, rigid, artificial aortic valves [24] and stented arteries [25]. The LBM is also suitable for modeling fluid-structure interactions since complex remeshing procedures for the fluid domain are not necessary. Fluid-structure interactions involving the LBM have so far been limited to either nondeformable structures, such as the simulation of particle-fluid suspensions [26–30] and artificial heart valves [31], or simple one-dimensional representations of the structure, i.e., the two-dimensional simulation of flow through a tube whose radius is assumed to be pressure dependent [32]. It is highly desirable, therefore, to couple the LBM with a numerical model of elastic mechanics that allows for deformable walls.

The lattice spring model consists of a network of harmonic springs that connect regularly spaced mass points. Through the correct choice of spring constants, this model can be directly mapped onto linear elasticity theory [11,33]. The main advantage of the LSM over alternative mechanical models is its computational efficiency and ease with which the deformation of highly heterogeneous systems can be simulated [8,34,35]. For example, the LSM has been shown to accurately capture the elastic fields that correspond to Eshelby's well-known theoretical solutions for the elastic behavior of an inhomogeneous material [11] and has been successfully used to simulate the deformation of multiparticulate systems [34–38]. We therefore adopt the LSM as the mechanical model to couple with the LBM. In this manner, simulations of fluid-structure interactions exploit the computational efficiency of both the LBM and LSM techniques.

In Sec.II, we detail the governing equations for both techniques, and discuss how the two models are integrated to yield our new approach. Section III describes our findings that are obtained with this integrated approach. We validate the model by calculating the "breathing mode" oscillations in an elastic shell filled with a Newtonian fluid, and comparing our results with analytic solutions. We then utilize the model to examine the interaction between an encapsulated fluid and a flat substrate. In particular, we vary the elastic constants of the shell, the viscosity of the fluid and the interaction potential between the microcapsule and the substrate. The findings provide insight into the role that each of the variables plays in the adhesion of the capsule to a specified surface. Consequently, the results can provide guidelines for designing microcapsules that bind to specific substrates.

II. METHODOLOGY

A. Lattice Boltzmann model

The lattice Boltzmann model is a lattice-based method for simulating hydrodynamic flows. The simulations consist of two processes, the first being the propagation of fluid "particles" to neighboring lattice sites and the second being collisions between particles when they reach a site. Here, fluid particles are representative of mesoscopic portions of the fluid, and are described by a particle distribution function; we use the term mesoscopic to represent a length scale between that of atomistic systems and continuum systems. The time evolution of this particle distribution function is governed by the discretized Boltzmann equation [39]

$$f_i(\mathbf{r}+\mathbf{e}_i\Delta t, t+\Delta t) = f_i^{\star}(\mathbf{r},t) = f_i(\mathbf{r},t) + \Omega_i[\mathbf{f}(\mathbf{r},t)], \qquad (1)$$

where $f_i(\mathbf{r},t) \equiv f(\mathbf{r},\mathbf{e}_i,t)$ describes the density of fluid particles at position $\mathbf{r}$ and time t, with a velocity $\mathbf{e}_i$. Here, $\mathbf{r}$, $\mathbf{e}_i$ and t are discrete variables, but the distribution function itself is continuous. To illustrate the two separate steps (collisions and propagation), we define $f_i^{\star}(\mathbf{r},t)$ as the post-collision particle distribution function.

The velocity $\mathbf{e}_i$ in the ith direction is chosen such that fluid particles propagate from one lattice site to the next in exactly one time step Δt (i.e., a distance of $|\mathbf{e}_i\Delta t|$). The 19 velocities of our three-dimensional model (often termed D3Q19) correspond to rest particles ($\mathbf{e}=[000]$), and to movement to the nearest- ($\mathbf{e}=\{100\}$) and next-nearest- ($\mathbf{e}=\{110\}$) neighbor directions of a simple cubic lattice. In the actual simulations presented here, both the lattice spacing Δx and the time step Δt are taken to be unity.

The collision operator $\Omega_i[\mathbf{f}(\mathbf{r},t)]$, accounts for the change in f_i due to instantaneous collisions at the lattice nodes; its action depends on all the f_i's at a node, denoted collectively by $\mathbf{f}(\mathbf{r},t)$. We adopted a multirelaxation time collision operator [40], which, in contrast to the more widely employed single relaxation time collision operator, enables us to assign independent values for both the shear and bulk viscosities (see Appendix A). External forces can be incorporated in the collision step in order to mimic gravitational forces or an

externally applied pressure gradient; however, such influences are not relevant to our study.

The hydrodynamic quantities, mass density ρ, momentum density $\mathbf{j}$, and the momentum flux $\mathbf{\Pi}$, are moments of the distribution function

$$\rho = \sum_i f_i,$$

$$\mathbf{j} = \sum_i f_i \mathbf{e}_i = \rho \mathbf{v},$$

$$\mathbf{\Pi} = \sum_i f_i \mathbf{e}_i \mathbf{e}_i. \tag{2}$$

Here, $\mathbf{v}$ is the local fluid velocity. In the LBM, these quantities evolve toward local equilibrium. For flow velocities much less than the speed of sound, the local equilibrium distribution function can be obtained by expanding the Maxwell-Boltzmann distribution as a Taylor series in the local velocity $\mathbf{v}$, i.e.,

$$f_i^{\mathrm{eq}} = \rho a_i \left[1 + \frac{\mathbf{v}\cdot\mathbf{e}_i}{c_f^2} + \frac{\mathbf{vv}:(\mathbf{e}_i\mathbf{e}_i - c_f^2\mathbf{I})}{2c_f^4} \right], \tag{3}$$

where $c_f^2 = c^2/3$, with $c = \Delta x/\Delta t$, and c_f is the isothermal speed of sound in the fluid; $\mathbf{I}$ is the unit tensor. The weights a_i only depend on the magnitude of the velocity $|\mathbf{e}_i|$ and are equal to $\frac{1}{3}$, $\frac{1}{18}$, and $\frac{1}{36}$ for the rest particles, the nearest-neighbor, and the next-nearest-neighbor directions, respectively. The expansion in Eq. (3) is truncated at $O(\mathbf{v}^2)$, which turns out to be sufficient to simulate the Navier-Stokes equation [41]. The second moment of the equilibrium distribution function gives the familiar Eulerian expression for the stress tensor

$$\mathbf{\Pi}^{\mathrm{eq}} = \sum_i f_i^{\mathrm{eq}} \mathbf{e}_i \mathbf{e}_i = p\mathbf{I} + \rho \mathbf{vv}, \tag{4}$$

with an ideal-gas equation of state $p = \rho c_f^2$.

Mass and momentum are conserved in the collision process; hence $\Sigma_i f_i = \Sigma_i f_i^{\mathrm{eq}}$ and $\Sigma_i f_i \mathbf{e}_i = \Sigma_i f_i^{\mathrm{eq}} \mathbf{e}_i$, as can be readily verified from Eqs. (2) and (3). However, the momentum flux is modified by the collision operator. In particular, the nonequilibrium stress tensor $\mathbf{\Pi}^{\mathrm{neq}} \equiv \mathbf{\Pi} - \mathbf{\Pi}^{\mathrm{eq}}$, is modified according to Eq. (A1) (see Appendix A), resulting in a post-collision nonequilibrium stress tensor that is given by [28]

$$\mathbf{\Pi}^{\mathrm{neq},\star} = (1+\lambda)\overline{\mathbf{\Pi}}^{\mathrm{neq}} + \frac{1}{3}(1+\lambda_B)(\mathbf{\Pi}^{\mathrm{neq}}:\mathbf{I})\mathbf{I}. \tag{5}$$

Here, λ and λ_B are relaxation parameters that appear in the collision operator. They control the relaxation of the fluid toward equilibrium and determine the shear and bulk viscosities of the fluid. The term $\mathbf{\Pi}^{\mathrm{neq}}:\mathbf{I}$ is the trace, and $\overline{\mathbf{\Pi}}^{\mathrm{neq}} = \mathbf{\Pi}^{\mathrm{neq}} - \frac{1}{3}(\mathbf{\Pi}^{\mathrm{neq}}:\mathbf{I})\mathbf{I}$ is the deviatoric part of the nonequilibrium stress tensor.

Using Eq. (5) for the post-collision nonequilibrium stress tensor, we can write the post-collision distribution function $f_i^\star$ defined in Eq. (1), as [28]

$$f_i^\star = a_i \left[\rho + \frac{\mathbf{j}\cdot\mathbf{e}_i}{c_f^2} + \frac{(\rho\mathbf{vv} + \mathbf{\Pi}^{\mathrm{neq}\star}):(\mathbf{e}_i\mathbf{e}_i - c_f^2\mathbf{I})}{2c_f^4} \right]. \tag{6}$$

We emphasize that the collision process locally conserves both mass and momentum, but relaxes the stresses toward local equilibrium. We also emphasize that as the fluid evolves toward equilibrium, the relaxation of the deviatoric and hydrostatic portions of the stress tensor occurs independently. This separation of relaxation times enables us to vary independently the shear viscosity η and bulk viscosity η_B [28], which are given by

$$\frac{\eta}{\rho} = -c_f^2 \left(\frac{1}{\lambda} + \frac{1}{2} \right) \Delta t,$$

$$\frac{\eta_B}{\rho} = -c_f^2 \left(\frac{2}{3\lambda_B} + \frac{1}{3} \right) \Delta t. \tag{7}$$

This allows us to simulate the hydrodynamics of Newtonain fluids with a wide range of shear and bulk viscosities.

B. Lattice spring model

The solid elastic material is represented by a rotationally invariant Hookean lattice spring model, consisting of a network of harmonic springs that connect regularly spaced mass points or nodes. The elastic energy associated with the ith node is given by

$$E_i = \frac{k}{2} \sum_j (|\mathbf{r}_{ij}| - |\mathbf{r}_{ij}^0|)^2, \tag{8}$$

where the summation runs over all nearest and next-nearest neighbor nodes, i.e., over all {100} and {110} bonds of an initially cubic lattice. Here, $|\mathbf{r}_{ij}|$ is the distance between the ith and jth nodes, $|\mathbf{r}_{ij}^0|$ is the equilibrium spring length and k is the spring constant [42]. (Note that using a cubic lattice consisting only of {100} bonds is insufficient for capturing isotropic elastic behavior [11].) This results in a force $\mathbf{F}_{ij}$ due to an extension or contraction of the spring connecting nodes i and j of the form

$$\mathbf{F}_{ij} = -\frac{\partial E_i}{\partial \mathbf{r}_{ij}} = -k \left(\frac{|\mathbf{r}_{ij}| - |\mathbf{r}_{ij}^0|}{|\mathbf{r}_{ij}|} \right) \mathbf{r}_{ij}. \tag{9}$$

For small deformations, this system of equations can be shown to obey linear elasticity theory and results in a Young's modulus $E = 5k/2\Delta x$. This simple model is restricted to a Poisson's ratio of $\nu = 1/4$ [43,44], although more complicated many-body interactions can be included in order to vary ν [45,46].

To capture the dynamics of this system, we must assign masses to the nodes and integrate Newton's equation of motion

$$\mathbf{F}_i = M_i \frac{\partial^2 \mathbf{r}_i}{\partial t^2}, \tag{10}$$

with M_i the mass of the node i and $\mathbf{F}_i$ the force acting upon it. We utilize the velocity Verlet algorithm to integrate Eq. (10). This is a well-known molecular dynamics algorithm

that uses the positions, velocities, and accelerations at time t to obtain the same quantities at time $t+\Delta t$ in the following way [47]:

$$\mathbf{r}_i(t+\Delta t) = \mathbf{r}_i(t) + \mathbf{v}_i(t)\Delta t + \frac{1}{2}\mathbf{a}_i(t)\Delta t^2,$$

$$\mathbf{v}_i\left(t+\frac{\Delta t}{2}\right) = \mathbf{v}_i(t) + \frac{1}{2}\mathbf{a}_i(t)\Delta t,$$

$$\mathbf{a}_i(t+\Delta t) = \frac{\mathbf{F}_i(t)}{M_i}$$

$$\mathbf{v}_i(t+\Delta t) = \mathbf{v}_i\left(t+\frac{\Delta t}{2}\right) + \frac{1}{2}\mathbf{a}_i(t+\Delta t)\Delta t, \qquad (11)$$

where $\mathbf{v}_i$ and $\mathbf{a}_i$ are the velocity and acceleration node i. Therefore, given applied forces and initial deviations from equilibrium, the dynamic evolution of the material, including the propagation of undamped elastic waves, can be accurately captured. Damping can be incorporated, for example, through the inclusion of a viscous damping term proportional to the velocity, but will not be considered here.

C. Solid-fluid coupling

In order to capture the fluid-structure interactions, LSM nodes that are situated near the solid-fluid interface must impose velocities on the enclosed fluid through boundary conditions and, in turn, experience forces due to the fluid pressure and viscous stresses. First, however, we must decide which LBM nodes are "solid" and which are "fluid." The masses at the LSM nodes represent mesoscopic portions of the elastic material. We can, therefore, define "solid LBM" nodes as nodes within close proximity (half the equilibrium [111] lattice length) of a LSM node. All other nodes are consequently "fluid LBM" nodes. This situation is depicted in Fig. 1, which shows a two-dimensional representation of a solid-fluid interface. The LSM lattice is represented by thick lines and the underlying LBM lattice is represented by thin lines. LBM nodes that lie within a given distance of a LSM node (represented by the dashed circles in the figure) are considered to be solid LBM nodes, while the remaining nodes are considered to be fluid LBM nodes.

This characterization implies that fluid LBM nodes are both created and destroyed as the LSM lattice deforms and moves with respect to the underlying LBM lattice (which is fixed in space). If the solid material moves, such that fluid nodes are created, then these nodes are assigned an equilibrium particle distribution function [see Eq. (3)] with a velocity equal to the local wall velocity [obtained in a manner similar to Eq. (13) below] and a mass density equal to the average local mass density of the neighboring fluid nodes. At this stage, we ignored the fact that for $\lambda \neq -1$ or $\lambda_B \neq -1$, this results in inaccuracies in the local shear stress. However, most of our simulations use relaxation parameters (λ's) of -1, resulting in a relaxation of the stresses in exactly one timestep [see Eq. (5)]. Hence, for these simulations, the post-collision distribution function is completely determined by only the mass density and the velocity, making our implementation correct [see Eqs. (3) and (6) for $\mathbf{\Pi}^{\mathrm{neq},\star}=0$]. We note that this issue is not unique to our approach, but an inherent problem of the link bounce-back rule and present in any system with moving boundaries, as for example, in particle suspensions [28,48]. We also note that it is possible to use interpolation to obtain the nonequilibrium particle distribution function [49], but we have not yet implemented this idea [50].

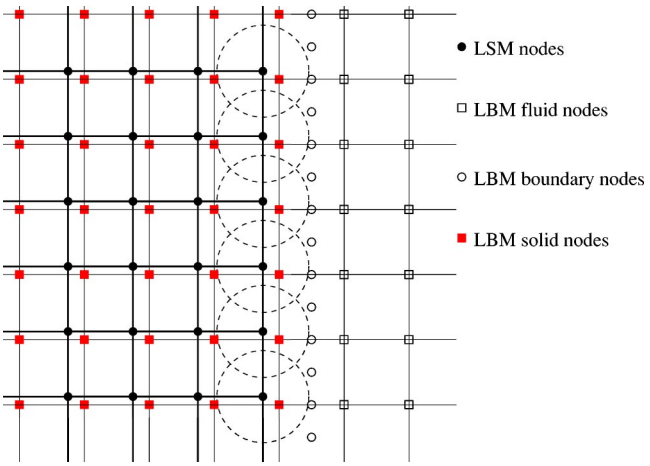

FIG. 1. (Color online) Two-dimensional representation of the solid-fluid boundary. The lattice spring lattice is depicted by thick lines while the lattice Boltzmann lattice is represented by thin lines. Solid LBM nodes are defined as being nodes within a given distance of a LSM node (shown here as dashed circles around LSM surface nodes). The remaining LBM nodes are then defined as fluid nodes. Boundary nodes are located halfway on links connecting fluid and solid nodes.

Fluid nodes that are destroyed are simply removed from the fluid phase in a way discussed in detail by Nguyen and Ladd [48]. This results in a rate of fluid mass that is destroyed (created) being equal to the rate at which mass is introduced (removed) in the system as a result of the link bounce-back scheme [see Eq. (12) below], with an error that is due only to a finite compressibility. However, the LBM is applicable only to systems with sufficiently small compressibility, thus minimizing this effect. In our simulations, we checked the rate at which fluid mass is globally created or destroyed and found the lack of global mass conservation to be negligible.

The fluid interacts with the surrounding solid via the so-called link bounce-back rule. This particular implementation of the no-slip boundary condition at the solid-fluid interface is robust, relatively simple, obeys global mass conservation, and does not require surface normals or tracking of the actual three-dimensional solid-fluid boundary. Its main disadvantage is its first order accuracy in the spatial discretization, a shortcoming that can be minimized by a calibration of the effective location of the boundary [26,28] or by using a particular set of eigenvalues of the collision operator [51]. For improved bounce-back schemes as well as references to other implementations we refer to a recent paper by Ginzburg and d'Humieres [51].

In the link bounce-back scheme, the solid-fluid interface is represented by LBM boundary nodes, defined as points in

space that are located halfway on each link that connects neighboring solid and fluid LBM nodes (see Fig. 1). Fluid particles that are being propagated toward a boundary node (in the i direction) are then reflected back in the direction they came from and modified such that [26],

$$f_k(\mathbf{r},t+\Delta t) = f_i^{\star}(\mathbf{r},t) - \frac{2\rho a_i \mathbf{e}_i \cdot \mathbf{v}_b(\mathbf{r}_b)}{c_f^2}, \tag{12}$$

where k is the direction opposite to i, and $\mathbf{v}_b(\mathbf{r}_b)$ is the velocity of the boundary node situated at $\mathbf{r}_b=\mathbf{r}+\mathbf{e}_i/2$. In order to obtain this velocity, we perform a weighted average of the velocities at the surrounding LSM nodes, i.e.,

$$\mathbf{v}_b(\mathbf{r}_b) = \frac{\sum_{\mathbf{r}}\left[\mathbf{v}(\mathbf{r})/(\mathbf{r}-\mathbf{r}_b)^2\right]}{\sum_{\mathbf{r}}\left[1/(\mathbf{r}-\mathbf{r}_b)^2\right]}, \tag{13}$$

where $\mathbf{r}$ and $\mathbf{v}(\mathbf{r})$ are the position and velocity of a neighboring LSM node, and the summation is taken to be over LSM nodes within a cutoff distance D. Hence, the closer a LSM node lies to a boundary node, the larger its contribution in defining the boundary node velocity. Here, the particular $(\mathbf{r}-\mathbf{r}_b)^{-2}$ weighting is chosen for convenience. The optimal value of D depends on the resolution of the underlying lattices, but has to be large enough to prevent unphysical fluctuations in the boundary node velocities. These velocities are, on the other hand, not very sensitive to the precise value of D due to our choice of the weighting function and we found the results to be nearly independent of D for $D \geqslant 3\Delta x$. In the simulations presented here, we used $D=5\Delta x$.

As a result of the bounce-back rule, the fluid exerts a force on the solid-fluid interface. This force is taken to be equal to the rate of exchange in momentum that takes place as the fluid particles are bounced back at the boundary nodes. The contribution from a single bounce-back event is of the form

$$\begin{aligned}\mathbf{F}_b\left(\mathbf{r}_b, t+\frac{\Delta t}{2}\right) &= f_i^{\star}(\mathbf{r},t)\mathbf{e}_i - f_k(\mathbf{r},t+\Delta t)\mathbf{e}_k \\ &= 2\left(f_i^{\star}(\mathbf{r},t) - \frac{\rho a_i \mathbf{e}_i \cdot \mathbf{v}_b(\mathbf{r}_b)}{c_f^2}\right)\mathbf{e}_i. \end{aligned} \tag{14}$$

In the applications discussed in this paper, we assume that, at equilibrium, the elastic shell does not inflate due to the presence of the enclosed fluid. Hence, to obtain the applied force, we subtract the equilibrium pressure due to the presence of the fluid at rest, i.e.,

$$\overline{\mathbf{F}}_b\left(\mathbf{r}_b, t+\frac{\Delta t}{2}\right) = \mathbf{F}_b\left(\mathbf{r}_b, t+\frac{\Delta t}{2}\right) - 2\rho_0 a_i, \tag{15}$$

with ρ_0 being the equilibrium density. This force acts on the boundary nodes of the LBM lattice and must therefore be distributed among the neighboring LSM nodes. Once again, a convenient choice is to weight these contributions inversely by the square of the distance between the boundary nodes and the neighboring LSM nodes. Hence, the total force on each LSM node is of the form

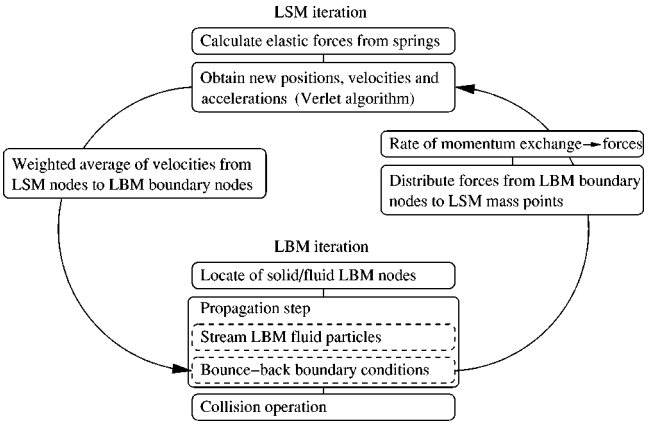

FIG. 2. Flowchart depicting the coupling between the lattice Boltzmann model and lattice spring model. A LSM iteration consists of calculating the elastic forces and the solid-fluid stresses and updating the positions, velocities and accelerations of the LSM nodes using the Verlet algorithm. A LBM iteration consists of determining the locations of fluid and solid nodes, propagating fluid particles to neighboring nodes and having particles undergo collisions at each node. The propagation step consists of two parts (dashed boxes): free streaming of fluid particles to their neighboring nodes whenever these nodes are in the fluid domain and applying the bounce-back boundary condition otherwise. The velocity at the solid-fluid boundary is obtained from the Verlet algorithm and used in the LBM bounce-back boundary condition. Fluid forces are then obtained from this boundary condition and used as input for the LSM update.

$$\mathbf{F}(\mathbf{r}) = \sum_{\mathbf{r}_b} \overline{\mathbf{F}}_b(\mathbf{r}_b) \frac{1/(\mathbf{r}-\mathbf{r}_b)^2}{\sum_{\mathbf{r}} 1/(\mathbf{r}-\mathbf{r}_b)^2}, \tag{16}$$

where the summations, over both neighboring LSM nodes ($\Sigma_{\mathbf{r}}$) and boundary nodes ($\Sigma_{\mathbf{r}_b}$), are over nodes that are within a certain cutoff distance, again chosen to be five lattice spacings.

To summarize, the simulation proceeds through the iterative update of both the LSM and LBM systems. A flowchart of the coupling between these systems is shown in Fig. 2. The LSM system is updated by first calculating the forces that are acting on the LSM nodes, due to both the LSM springs and the enclosed fluid. The positions, velocities, and accelerations of the LSM nodes are then updated using the Verlet algorithm. In updating the LBM system, we first establish which LBM nodes are solid and which are fluid, and then obtain the location and the velocity of the LBM boundary nodes. Next, we propagate the distribution function by streaming fluid particles to their neighboring nodes whenever these nodes are in the fluid domain and applying the bounce-back boundary condition otherwise. Finally, we modify the distribution functions at the LBM nodes to account for the collision step. The bounce-back rule is implemented by using a boundary node velocity that is obtained from the velocities of the surrounding LSM nodes and returns the fluid forces that are acting on the solid-fluid interface. Hence, the fluid imposes stresses on the surrounding solid and the solid dictates the velocity of the fluid at the solid-fluid interface.

In this section, we have shown that it is possible to couple the LSM and the LBM, allowing for a dynamic interaction between the elastic material and the confined fluid. Furthermore, the speed of sound in the solid ($c_s=\sqrt{3k/M}\Delta x$) can be set relative to that in the fluid [$c_f=\sqrt{1/3}(\Delta x/\Delta t)$], allowing us to vary the ratio between the speeds of sound in the solid and fluid domain in order to meet the characteristics of an actual experiment. In the next section, we validate the coupled model and apply it to a study of the impact of a fluid-filled, elastic shell on a hard wall and on an adhesive surface.

III. RESULTS AND DISCUSSION

We investigate the dynamic behavior of an elastic, spherical shell that is filled with a Newtonian fluid. First, we consider the "breathing-mode" oscillations of this system and compare our results with analytical solutions. Next, we consider the fate of a fluid-filled, elastic shell impacting a hard surface and bouncing back in the opposite direction. Finally, we simulate the impact and cohesion of a fluid-filled shell on an adhesive wall in order to gain an understanding of how the capsule-wall interactions affect the dynamical behavior.

A. Breathing-mode oscillations of a spherical shell

We validate our coupled model by comparing our results for the oscillatory behavior of an elastic shell, both *in vacuo* and when filled with a Newtonian fluid, with theoretical predictions (see Appendix B). Initially, we deform the shell such that it is radially expanded; we then study the response of the system by allowing the shell to relax toward its equilibrium, undeformed state. Following the initial expansion, the system will contract and expand in an oscillatory manner ("breathing mode") with a characteristic frequency. For an elastic shell *in vacuo* these oscillations are undamped, and the lowest frequency is given by

$$\omega_0=\left(\frac{1}{R}\right)\left[\frac{2E}{\rho_s(1-\nu)}\right]^{1/2}\left[1+O\left(\frac{h^2}{R^2}\right)\right]. \tag{17}$$

Here, R is the middle radius of the shell, h its thickness, E its Young's modulus, ρ_s its density, and ν its Poisson's ratio. The leading term was first obtained by Lamb [52] [see also Eqs. (B3) and (B25)]. Corrections to this term are small and usually ignored; they are of order $(h/R)^2$ and result in a relative increase in ω_0 of only 1.6% for $h/R=0.5$ [as obtained from Eq. (B23) for $\nu=1/4$].

First, we test the LSM by calculating the breathing-mode frequency of an elastic shell *in vacuo* as a function of the shell's thickness. The middle radius of the shell R is taken to be 50 lattice sites, and we fix the Young's modulus and density of the shell at $E=67.5$ and $\rho_s=11.25$ (in lattice units), respectively. Remember that for our particular LSM, $E=5k/2\Delta x, \rho_s=M/(\Delta x)^3$, while the Poisson's ratio ν is restricted to $1/4$ (see Sec. II B). Hence, in the remainder of this paper, we will use the physical variables E and ρ_s, instead of the LSM variables k and M. The speed of sound in the shell is then given by $c_s=\sqrt{6E/5\rho_s}$, consistent with Eq. (B3) for $\nu=1/4$.

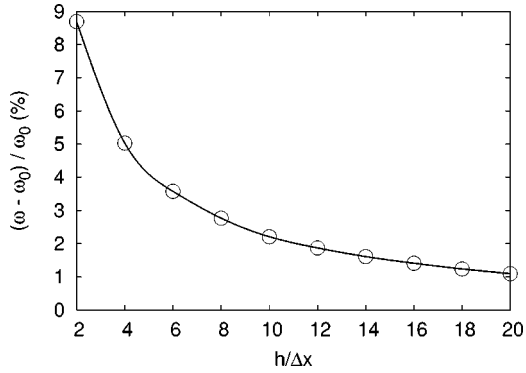

FIG. 3. Comparison of our simulation results with the analytical solution for the breathing-mode frequency of an elastic shell *in vacuo*. The percentage deviation of our simulation results ω from the analytical solution ω_0 are presented as a function of the shell thickness h. The circles mark the data points; the line is drawn as a guide for the eye.

Figure 3 depicts the percentage deviation in the breathing-mode frequency ω_0 between the simulation result and that obtained from the full analytical solution (B23) as a function of shell thickness h. For a thin shell of two lattice spacings, there is almost a 9% difference between the frequency of the simulated oscillation and the theoretical prediction. However, as we increase the shell thickness, the simulation results converge with the analytical solution. As the thickness of the shell is increased, a greater number of LSM nodes are employed in describing the elastic properties of the shell, minimizing discretization effects and, consequently, deviations from the theoretical prediction. For a shell thickness of ten lattice spacings, the simulation results are within 2% of the analytical solution. Therefore, we choose this thickness in the remainder of this paper.

Next, we test the coupled model by calculating the breathing-mode frequency of an elastic shell that is filled with a Newtonian fluid. We use the same numerical experiment of an initially radially perturbed system. To aid in visualizing the results, we plot a snapshot of the system in Fig. 4, showing both the elastic shell and confined fluid as the shell is expanding. For clarity, we only show the image for half of the system. The shell is colored red and the velocity of the fluid is represented by "cones" that point in the direction of fluid flow. The size of the cones depicts the magnitude of the velocity. Figure 4 clearly shows that the fluid moves radially outward as the shell expands, with a velocity that varies in the radial direction.

To quantify our observations on this system, we first measure the average radial displacement over all LSM nodes. Figure 5 shows the relative average radial displacement as a function of time (normalized with the period of oscillation $T_0=2\pi/\omega_0$ for an elastic shell *in vacuo*). A positive value corresponds to an expansion and a negative value to the contraction of the elastic shell. We use $E=25/16$ and $\rho_s=11.25$ (in lattice units), resulting in a ratio $c_s/c_f=1/\sqrt{2}$ between the speed of sound in the shell and that in the fluid. This ratio is small enough to ensure that we only excite a single frequency, in this case the lowest order breathing mode (see Fig. 6). The fluid density $\rho_f=1$, while $R=50$ and $h=10$, all in lattice units.

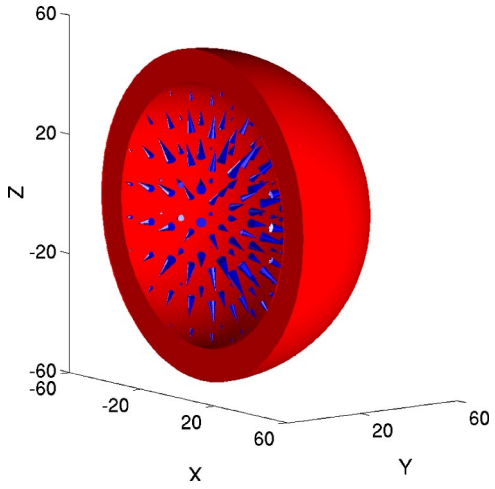

FIG. 4. (Color online) A fluid-filled shell undergoing breathing mode oscillations. The shell is colored red and the velocity of the fluid is depicted by blue cones whose size and orientation depict the magnitude and direction of the velocity field.

In order to assess the effect of the enclosed fluid on the oscillatory behavior of the elastic shell, we vary the bulk and shear viscosities of the fluid. Variations of the shear viscosity are found to have a negligible effect on the frequency of the breathing-mode oscillations. We therefore fix $\eta=1/6$ (in lattice units), i.e., $\lambda=-1$, ensuring instantaneous relaxation of the shearstresses to local equilibrium [see Eqs. (5) and (7)]. The bulk viscosity, however, has an appreciable influence on the oscillatory behavior of the elastic shell. This is to be expected since the breathing-mode oscillations change the total fluid volume enclosed by the shell, and the bulk viscosity controls the effect of this volume change on the resultant hydrostatic pressure inside the shell. We therefore focus on the effects of varying bulk viscosity in Fig. 5. It is clear that as the bulk viscosity is increased, the oscillations become more strongly damped; this is particularly evident from the diminishing amplitude for $\eta_B=40/6$. Figure 5 also shows a transition from weak damping to strong damping evident for

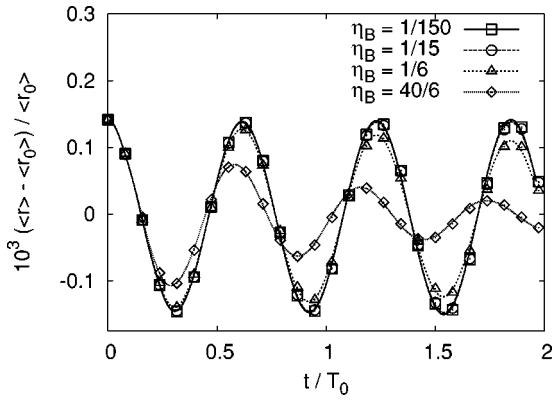

FIG. 5. The relative average radial displacement as a function of time for fluid-filled shells oscillating at their breathing mode frequency and containing fluids with varying bulk viscosities. Here, time is normalized with the period of oscillation of an elastic shell *in vacuo*.

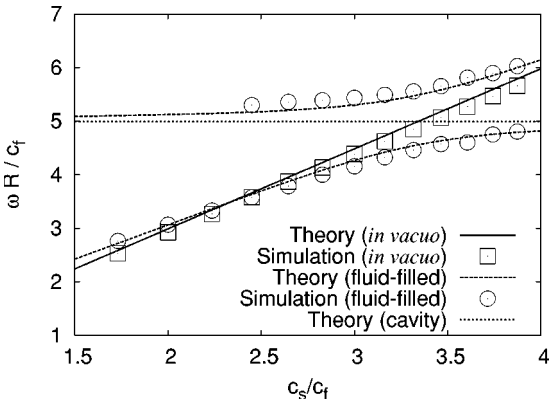

FIG. 6. The dimensionless breathing-mode frequency as a function of the ratio between the speeds of sound in the solid and the fluid. Here, c_f is fixed and c_s is varied by varying the Young's modulus of the elastic shell. Simulation results for both shells *in vacuo* (squares) and fluid-filled shells (circles) are compared with their theoretical predictions (lines).

a bulk viscosity of $\eta_B=40/6$, for which the frequency of the oscillations is affected by the value of the bulk viscosity, with the frequency increasing with increasing bulk viscosity.

We then compare our simulation results for the breathing-mode frequency with the analytical solution for an elastic shell filled with an inviscid fluid (see Appendix B). Here, the respective shear and bulk viscosities are taken to be $1/6$ and $1/9$ (in lattice units), ensuring that we are in the weak-damping limit, i.e., that the effect of the damping on the frequency of the oscillation is negligible (see Fig. 5). This makes comparing the frequencies with theoretical predictions for an inviscid fluid meaningful. We then vary the shell's Young's modulus to obtain results for a large range of ratios between the speed of sound in the shell and that in the fluid. All other shell and fluid properties are the same as given in the empty shell example above. Figure 6 compares the results from our simulations with the theoretical results obtained from Eq. (B27). The breathing-mode frequencies are nondimensionalized with the middle radius of the shell and the speed of sound in the fluid, and plotted as a function of the ratio between the speeds of sound in the shell and the fluid. For $c_s/c_f \gtrsim 2.5$ we clearly excite the two lowest breathing mode frequencies. Increasing c_s/c_f gradually increases the ratio of the amplitude of the second mode relative to that of the first mode, from 0.12 at $c_s/c_f=2.45$ to 2.8 at $c_s/c_f=3.87$. Contribution of higher order modes was negligible for the range of c_s/c_f in Fig. 6. Hence, the simulations clearly capture the lowest two branches of the breathing-mode frequency spectrum. Figure 6 also shows the results for the elastic shell *in vacuo* in the same nondimensional units. It illustrates that the breathing-mode frequency spectrum for the elastic shell filled with an inviscid fluid [Eq. (B27)] roughly resembles that of a superposition of that for an elastic shell *in vacuo* [Eq. (B23)] and that for an inviscid fluid in a rigid cavity [Eq. (B30)].

Figure 6 shows that the simulation results are in good agreement with the theoretical predictions, validating our technique. As a demonstration, we now turn our attention to investigating the collision between this fluid-filled, elastic shell, and a hard wall.

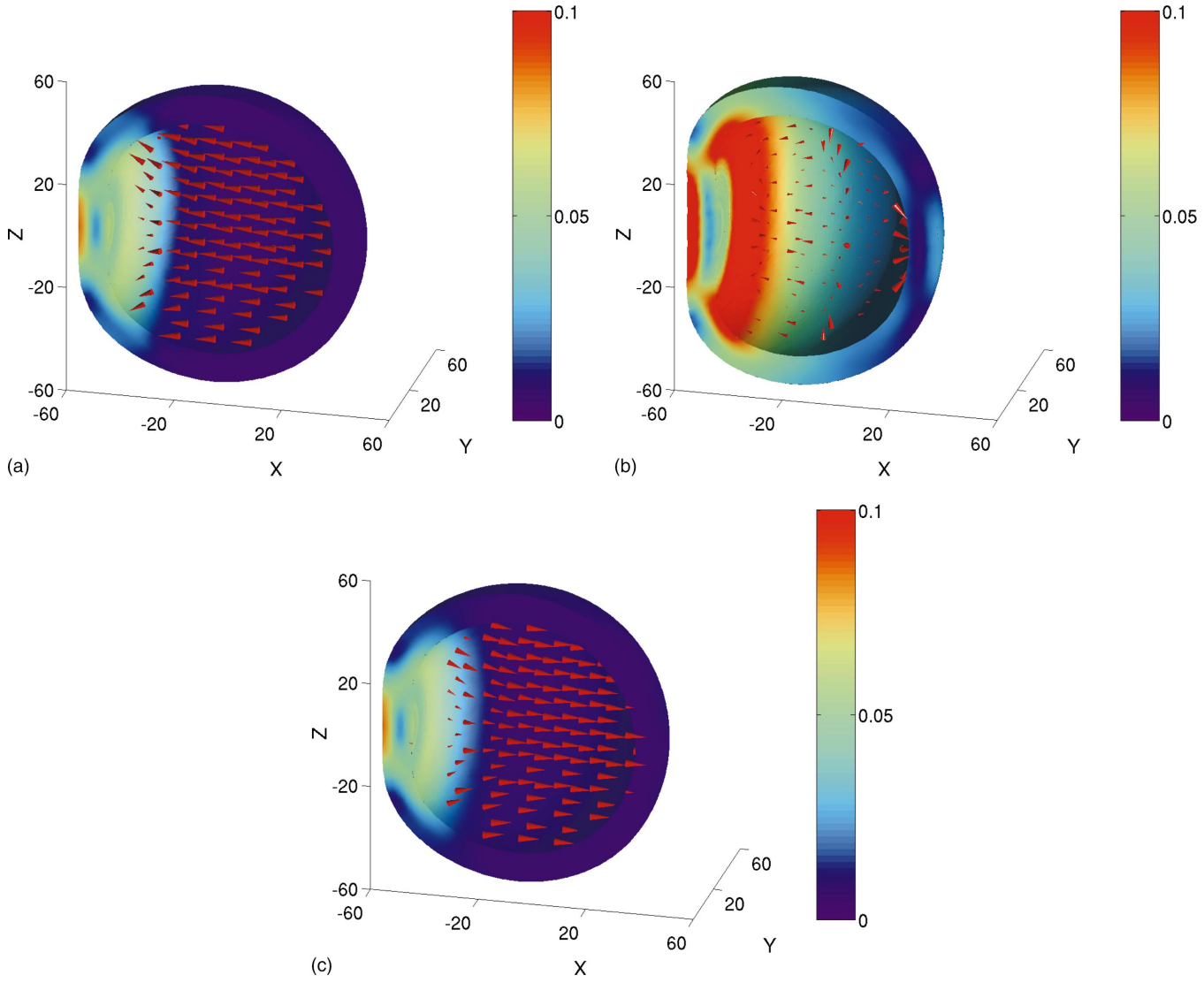

FIG. 7. (Color) Time frames showing the impact of a fluid-filled elastic shell on a hard wall at $t=200$ [(a), top, left], $t=600$ [(b), top, right], and $t=1000$ [(c), bottom]. The velocities in the fluid are depicted as red cones whose size and orientation represent the magnitude and direction of the velocity field. The size of the cones are scaled by a factor of 200 in (a) and (c), and 1500 in (b) in order for the cones to be visible. The shell colors are a measure for the equivalent strain in the solid domain.

B. Impact of a fluid-filled spherical shell on a hard wall

Here, we consider the impact of a fluid-filled shell on a hard wall in the *yz* plane, which we introduce through the use of a repulsive exponential potential that acts upon the LSM nodes. In particular, we mimic a hard wall by imposing a force on the LSM nodes of the form

$$F(x) = \begin{cases} \exp\left(\dfrac{-(r_x - r_{x,w})}{\sigma}\right), & r_x < -56, \\ 0, & r_x > -56. \end{cases} \tag{18}$$

Here r_x is the x coordinate of a LSM node, $r_{x,w}=-58$, and $\sigma=0.2;\sigma$ is a measure of the length scale of the sphere-wall interaction and is chosen to be much smaller than that of the lattice spacing (which is unity).

The dynamic behavior of a fluid-filled elastic shell as it impacts a hard wall is depicted in Fig. 7 [53]. The surface of the shell is colored to represent the elastic material's "equivalent strain," which is defined as $u_{\mathrm{eq}}=\sqrt{\frac{2}{3}u_{ij}u_{ij}}$, with u_{ij} being the strain tensor. The equivalent strain provides an isotropic scalar measure of the strain level. As indicated by the color bar in the figure, the regions that are most deformed are marked in red. The velocity of the fluid is again represented as cones that point in the direction of fluid flow and whose size depict the magnitude of the velocity. The elastic shell and the enclosed fluid are initially assigned the same velocity $v_x=-v_0$ as the capsule moves toward the wall and the system travels unperturbed until it reaches the wall. The magnitude of the initial velocity $v_0=0.02$ is roughly an order of magnitude smaller than the speed of sound in the fluid. Unless specifically mentioned otherwise, we use $E=25/16, \rho_s=11.25$ (giving $c_s/c_f=1/\sqrt{2}$), $R=50, h=10, \rho_f=1, \eta=1/6$, and $\eta_B=1/9$ (all in lattice units). Figure 7(a) depicts the shell as it reaches the hard wall. The shell de-

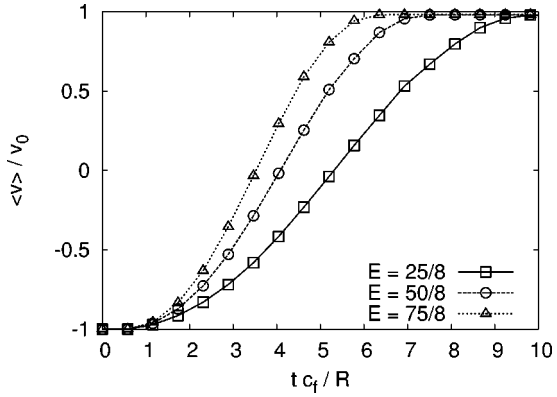

FIG. 8. The average velocity in an elastic shell *in vacuo* as a function of time as it impacts a hard wall, for shells of varying Young's modulus. The velocities are normalized with v_0 and time with R/c_f.

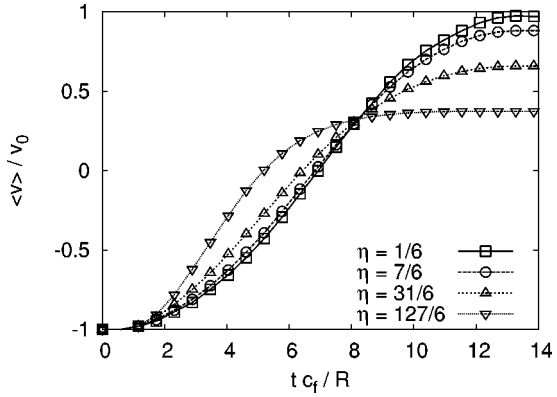

FIG. 9. The average velocity in an elastic shell *in vacuo* as a function of time as it impacts a hard wall, for shells containing fluids of varying shear viscosity. The velocities are normalized with v_0 and time with R/c_f.

forms as it impacts the wall due to the strong repulsive force. It becomes compressed at the region of impact (red part of the shell surface) and appears slightly flattened. The velocity of the shell in the region of impact is significantly decreased, while the velocity in the rest of the system is still close to the initial velocity.

Figure 7(b) depicts the shell at its maximum deformation, just as it starts to rebound off the hard wall. The kinetic energy of the moving system has largely been converted into elastic energy through the deformation of the shell. The regions that are most deformed are represented by red surfaces. For the selected parameters, the shell only appears to be significantly deformed in the region of impact. However, the rest of the shell is also deformed as it "bends" and becomes "squashed" or compressed as a result of the impact. In fact, the first regions that begin to recover are those farthest away from the region of impact (as indicated by the reversed velocity cones on the opposite side of the impact region), and those on the sides (as indicated by the inwardly pointing velocity cones).

The elastic energy stored in the deformed shell is transferred to kinetic energy as the elastic shell regains its original shape. Figure 7(c) shows the system just before the shell leaves the surface. The only region of noticeable deformation is the region of the shell that is still in contact with the hard wall. The rest of the shell has already regained its original shape. The velocity in the fluid is near zero near the region of the shell still in contact with the wall, but is directed away from the wall in the rest of the shell (with nearly the same magnitude as the velocity before impact).

In order to better understand this dynamic behavior, we first return to the simpler case of an elastic shell *in vacuo* and consider the effects of varying the Young's modulus on the shell's impact with a hard wall. Figure 8 shows the average velocity of the elastic shell, normalized with v_0, as a function of time, normalized with R/c_f. Increasing the Young's modulus has the effect of decreasing the amount of deformation in the elastic shell and, therefore, decreases the time it needs to recover its original shape. This can be seen in Fig. 8 from the time it takes for the average velocity to change from propagating toward the wall (negative velocity) to propagating away from the wall (positive velocity). It should be noted that the magnitude of the shell's velocity as it travels away from the wall is slightly lower than that of its initial velocity. This is due to energy being transferred upon impact to elastic deformations that propagate around the spherical shell; the shell effectively "rings" as it travels away from the wall. (In these simulations, these internal vibrations are undamped.)

With this insight into the behavior of an empty elastic shell, we return to the case of the fluid-filled, elastic shell to investigate the effects that the fluid properties have on the impact behavior of the system. As the shell impacts the hard wall, stresses act on the fluid in the region of impact, and these stresses are transferred to other regions of the fluid and the shell. The deformations appear to be relatively volume conserving for the parameters considered here and, as such, we expect little influence of the bulk viscosity on the impact behavior of the system. However, we expect significant gradients in the fluid's velocity field as the shell comes to a halt, and ultimately rebounds in the opposite direction. Hence, we anticipate a significant influence of the shear viscosity on the collision process. We varied both the shear and bulk viscosities, and found, indeed, that varying the bulk viscosity has a negligible effect compared to that of varying the shear viscosity. Hence, we fix the bulk viscosity to $1/9$ (in lattice units), i.e., $\lambda_B=-1$, ensuring instantaneous relaxation of the bulk-stresses to local equilibrium [see Eqs. (5) and (7)]. We then vary the shear viscosity, keeping all other variables fixed at the same values as for the empty shell simulations. Figure 9 shows the average velocity of the shell as a function of time, for shells containing fluids of different shear viscosities. As expected, increasing the shear viscosity increases the damping of the shell dynamics. In particular, the velocity of the shell decreases more rapidly, and the shell rebounds from the wall with a significantly lower velocity. The initial kinetic energy of the system is no longer primarily stored as elastic energy, but is now significantly dissipated by the fluid.

We have shown how the mechanical properties of the elastic shell and the viscous behavior of the enclosed fluid influence the dynamics of a fluid-filled shell impacting a hard wall. As noted in the Introduction, the binding of microcap-

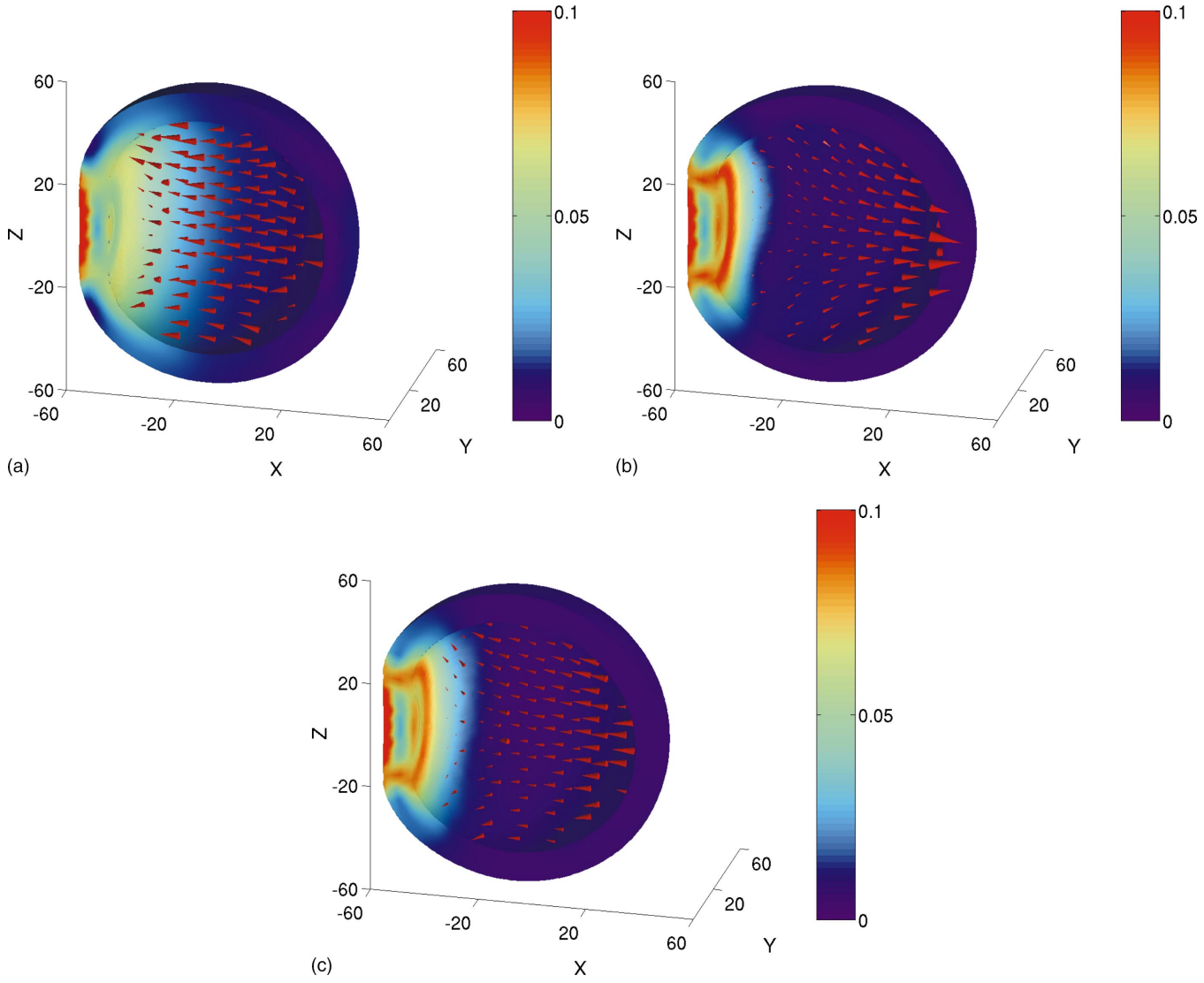

FIG. 10. (Color) Time frames showing the impact of a fluid-filled elastic shell on an adhesive wall at $t=300$ [(a), top, left], $t=600$ [(b), top, right], and $t=900$ [(c), bottom]. The velocities in the fluid are depicted as red cones whose size and orientation represent the magnitude and direction of the velocity field. The size of the cones are scaled by a factor of 500 in order for the cones to be visible.

sules onto surfaces can be essential to their functionality [13]; consequently, in the next section, we consider the impact of a fluid-filled elastic shell on an adhesive wall.

C. Impact of fluid-filled spherical shell on an adhesive wall

In order to mimic the "tackiness" of an adhesive wall in the *yz*-plane, we replace the exponential force used in the previous section to simulate a hard wall with a velocity-dependent force that can be either repulsive or attractive. For convenience we use a force that is defined through a potential

$$U(r_x)=\begin{cases}4\epsilon\left[\left(\dfrac{\sigma}{r_x-r_{x,w}}\right)^{12}-\left(\dfrac{\sigma}{r_x-r_{x,w}}\right)^{6}\right], & r_x<r_{x,c}\vee v_x>0,\\ 0, & r_x>r_{x,c}\wedge v_x<0.\end{cases} \tag{19}$$

Here r_x is the x coordinate of a LSM node, and v_x its velocity in the x direction; $r_{x,w}=-58$ is the x coordinate of the wall and σ and ϵ control the range and magnitude of the interaction. Note that the force changes sign at some value $r_x=r_{x,c}$, and that it is attractive for $r_x<r_{x,c}$ and repulsive for $r_x>r_{x,c}$. Equation (19) implies that as a LSM node approaches the wall, it experiences a purely repulsive interaction mimicking a hard wall; however, as it moves away from the wall, it experiences an attractive potential. In this manner, the shell experiences "tackiness" as it impacts the adhesive surface. We have set $\sigma=0.8$, fixing the range of the repulsive part of the potential $(r_{x,c}-r_{x,w})=\sigma 2^{1/6}\approx 1$.

Figure 10 captures the dynamic behavior of a fluid-filled, elastic shell impacting the adhesive wall [53]. Unless specifically mentioned otherwise, we use in this section $E=25/4, \rho_s=11.25$ (giving $c_s/c_f=\sqrt{2}$), $R=50, h=10, \rho_f=1, \eta=1/6, \eta_B=1/9$, and $v_0=0.02$ (all in lattice units). Figure 10(a) shows the shell as it impacts the wall. The velocity of the fluid is directed toward the wall and the deformation of the shell is localized in the region of impact. Similar to the impact of a fluid-filled shell on a hard wall, the shell deforms

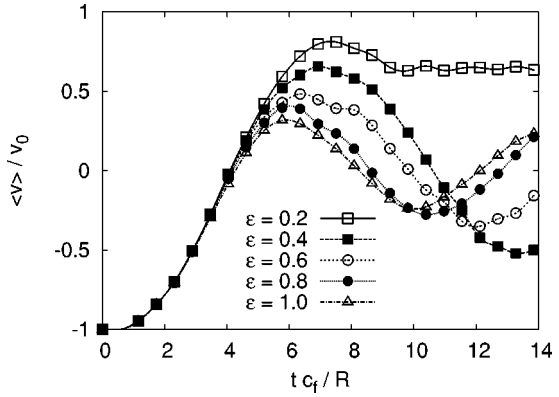

FIG. 11. The average velocity in a fluid-filled elastic shell as a function of time as it impacts an adhesive wall of varying interaction strength. The velocities are normalized with v_0 and time with R/c_f.

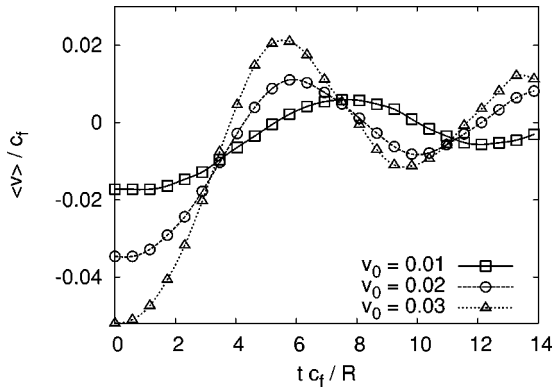

FIG. 12. The average velocity in a fluid-filled elastic shell as a function of time as it impacts an adhesive wall at varying velocity. The velocities are normalized with c_f and time with R/c_f.

upon impact, after which it comes to a halt. As the elastic energy stored upon impact is released in the form of kinetic energy, the shell begins to move away from the wall. This is shown in Fig. 10(b), where the system starts to move away from the wall in the regions that lie opposite to the area of impact. In the region of impact, however, the velocity remains essentially zero as the shell adheres to the wall. Hence, the shell stretches out, trying to pull away from the wall, but remains "stuck" if the adhesive force is large enough (as is the case in Fig. 10). The elastic energy in the shell increases as the nonadhered portions become elongated away from the wall, pulling the shell back toward the wall [see Fig. 10(c)]. The system then starts to oscillate between these two states; either squashed against the wall or elongated away from it.

First, we study the effect of varying the interaction strength between the fluid-filled shell and the adhesive wall. In particular, the value of the interaction parameter ϵ in Eq. (19), is varied from 0.2 to 1.0 (in lattice units). Figure 11 shows the average velocity of the shell as a function of time. Whether the shell rebounds off the wall, and how, is affected by the attractive interaction with the wall. For $\epsilon=0.2$, the adhesive force slows down the shell as it moves away from the wall, but the attraction is too small to bind the shell to the wall. For higher values of ϵ, the adhesion is strong enough to bind the particle to the wall, and the shell starts to oscillate between a "squashed" state and an "elongated" state in a manner close to that depicted in Fig. 10. As the interaction strength is increased, two things occur: the amplitude of the oscillations in the averaged velocity decreases, and their frequency increases. The increase in interaction strength increases the area of adhesion, thus limiting the regions of the shell that are free to vibrate. The greater the area of a shell that is adhered to the surface, the higher the frequency of oscillation. This is consistent with Eq. (17), which does in fact indicate that smaller shells oscillate at a higher frequency.

A similar phenomenon occurs when the shell impacts the adhesive wall at different initial velocities. Figure 12 shows the average velocity, normalized with c_f, as a function of time, for shells that impact the adhesive wall with initial velocities v_0 of 0.01, 0.02, and 0.03. Here, we fix $\epsilon=1$. The most notable feature is that the frequency of the oscillations of the adhered shell increases as the speed with which the shell impacts the adhesive wall is increased. The shell undergoes greater deformation as it impacts the wall at a higher speed, resulting again in a larger region of the shell being adhered to the wall, and increasing the frequency of the oscillations.

Next, we investigate the effects of varying the Young's modulus of the shell on the dynamics of the fluid-filled shell impacting an adhesive wall. Figure 13 shows the average velocity as a function of time. Similar to Fig. 8, an increase in the Young's modulus generally results in a decrease in the amount of deformation and hence a decrease in the area of contact, enabling the shell to regain its original shape in less time. Figure 13 shows that when the adhesion is strong enough, the shell adheres to the wall and starts to oscillate with a frequency that increases with increasing Young's modulus. This frequency dependence on Young's modulus is qualitatively similar to that of the breathing mode vibrations of an elastic shell *in vacuo* as given by Eq. (17).

Finally, Fig. 14 shows the effects of varying the shear viscosity of the enclosed fluid. In particular, we plot the average velocity of the shell as a function of time for shells

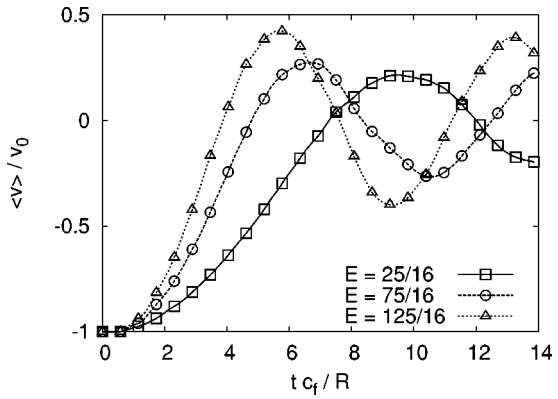

FIG. 13. The average velocity in a fluid-filled elastic shell as a function of time as it impacts an adhesive wall, for shells of varying Young's modulus. The velocities are normalized with v_0 and time with R/c_f.

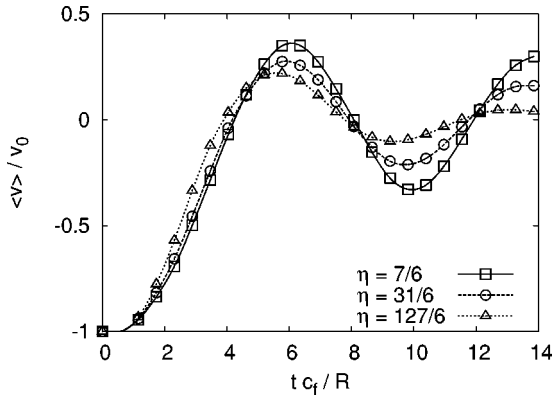

FIG. 14. The average velocity in a fluid-filled elastic shell as a function of time as it impacts an adhesive wall, for shells containing fluids of varying shear viscosity. The velocities are normalized with v_0 and time with R/c_f.

containing fluids with shear viscosities $\eta=7/6,31/6$, and $127/6$. As the shear viscosity is increased, the oscillations become increasingly damped, in a way that is qualitatively similar to the situation of a fluid-filled, elastic shell impacting on a hard wall (see Fig. 9).

IV. CONCLUSIONS

In summary, by coupling the lattice spring model (LSM) of elastic mechanics and the lattice Boltzmann method (LBM) for fluid dynamics, we have developed a flexible, robust, and relatively simple method for solving fluid-structure interactions. In this paper, we demonstrated the validity of this approach by simulating the breathing mode oscillations of an elastic, fluid-filled spherical shell and comparing the results with analytical solutions. We find good, quantitative agreement between the simulation and analytical results. Furthermore, we demonstrated the utility of the approach by investigating the impact of a fluid-filled shell on two types of surfaces: hard (purely repulsive) and adhesive. We showed that for a range of operating conditions, the resultant dynamic behavior is sensitive to both the elastic properties of the shell and the viscous properties of the enclosed fluid. A fundamental understanding of the dynamics of fluid-filled shells is particularly important in the design of effective microcapsules for pharmaceutical or other commercial applications. Our studies reveal that the physical properties of both the outer casing and the inner fluid can play a role in controlling the binding of these capsules to the specified surfaces.

In future studies, we will exploit the capabilities of this approach to examine other types of problems that require an efficient method for simulating fluid-structure interactions. In particular, we will consider the flow of fluids in compliant pipes or tubes. Through the LSM, we can introduce mechanical heterogeneities along the length of the pipe by making some portions of the pipe stiffer than others, or in the radial direction by making the tube stiffer as one moves from the inner to the outer surface. Furthermore, through the LBM, we can consider not only single-component fluids, but also multicomponent liquids or liquid-gas mixtures. Modeling the flow of complex fluids through laterally or radially heterogeneous pipes is important for various scientific and engineering applications. If the tubes are constructed to represent biological systems, we can use the simulations to probe blood flow in capillaries or air flow through compartments in the lungs. Thus, the integrated LBM-LSM model opens up the possibility of accurately and efficiently capturing dynamic interactions between fluid flow and structural interactions in a broad variety of systems.

ACKNOWLEDGMENTS

The authors gratefully acknowledge financial support from ONR, ARO, and DOE.

APPENDIX A: THE LBM COLLISION OPERATOR

The time evolution of the particle distribution function is governed by the discretized Boltzmann equation, where the collision operator $\Omega_i[\mathbf{f}(\mathbf{r},t)]$, accounts for the change in f_i due to instantaneous "molecular" collisions at the lattice nodes [see Eq. (1)]. A computationally useful form for the collision operator can be constructed by linearizing about the local equilibrium distribution function [54]

$$\Omega_i[\mathbf{f}(\mathbf{r},t)] = \sum_j \mathcal{L}_{ij}[f_i(\mathbf{r},t) - f_i^{\mathrm{eq}}(\mathbf{r},t)], \tag{A1}$$

where $\mathcal{L}_{ij}$ are the matrix elements of the linearized collision operator $\mathcal{L}$. This linearized collision operator must satisfy the following eigenvalue equations:

$$\sum_i \mathcal{L}_{ij} = 0,$$

$$\sum_i \mathbf{e}_i \mathcal{L}_{ij} = 0,$$

$$\sum_i \overline{\mathbf{e}_i \mathbf{e}_i} \mathcal{L}_{ij} = \lambda \overline{\mathbf{e}_j \mathbf{e}_j},$$

$$\sum_i e_i^2 \mathcal{L}_{ij} = \lambda_B e_j^2, \tag{A2}$$

where $\overline{\mathbf{e}_i \mathbf{e}_i}$ indicates the deviatoric part of $\mathbf{e}_i \mathbf{e}_i$. The first two equations follow from conservation of mass and momentum [see Eq. (1)], and the last two equations describe the isotropic relaxation of the viscous stress tensor; the eigenvalues λ and λ_B are related to the shear and bulk viscosities [see Eq. (7)], and must lie in the range $(-2,0)$. Equation (A1) accounts for ten of the eigenvectors of $\mathcal{L}$ (six in two dimensions). The remaining nine (three in two dimensions) modes are higher-order eigenvectors of $\mathcal{L}$ that are not relevant to the Navier-Stokes equations, but which do affect the boundary conditions at the solid-fluid interfaces. In general the eigenvalues of these kinetic modes are set to -1 , which both simplifies the simulation and ensures a rapid relaxation of the nonhydrodynamic modes [26].

The collision operator can be further simplified by taking a single eigenvalue for both the viscous and nonhydrodynamic kinetic modes [55,56]. This (single) exponential relax-

ation time (ERT) approximation, $\Omega_i=-(f_i-f_i^{\mathrm{eq}})/\tau$, has become the most popular form for the collision operator because of its simplicity and computational efficiency. However, the absence of a clear time scale separation between the hydrodynamic and nonhydrodynamic modes reduces the numerical stability [40,57], and can sometimes cause significant errors at solid-fluid boundaries [28]. Furthermore, it does not allow independent variation of the bulk and shear viscosities. Thus we employ the more flexible collision operator of Eq. (A1).

APPENDIX B: BREATHING-MODE OSCILLATIONS OF A SPHERICAL SHELL

Here we summarize the theoretical analysis of the oscillatory behavior of an elastic shell, both *in vacuo* and when filled with an inviscid fluid. We limit ourselves to the response of the system after an initial radial expansion. Following the initial expansion, the system will contract and expand in an oscillatory manner ("breathing mode") with a characteristic frequency. Because of the symmetry of the system the breathing mode is completely described by the radial component of the displacement vector $u_r(r,t)$ in the shell, and the radial component of the enclosed fluid velocity $v_r(r,t)$, which furthermore only depend on the radial coordinate r and time t. We denote the radius of the outer surface of the shell with a, that of the inner surface with b, while $R=(a+b)/2$ and $h=a-b$.

The displacement vector $\mathbf{u}(\mathbf{r},t)$ in the shell is determined by the equation of motion for an isotropic elastic medium (e.g., Ref. [58]),

$$\rho_s\frac{\partial^2\mathbf{u}}{\partial t^2}=\frac{E}{2(1+\nu)}\boldsymbol{\nabla}^2\mathbf{u}+\frac{E}{2(1+\nu)(1-2\nu)}\boldsymbol{\nabla}\,\boldsymbol{\nabla}\cdot\mathbf{u}, \tag{B1}$$

with E the shell's Young's modulus, ρ_s its density, and ν the Poisson's ratio. Hence, for $\mathbf{u}(\mathbf{r},t)=u_r(r,t)\hat{\mathbf{r}}$, with $\hat{\mathbf{r}}$ the unit vector in the radial direction, Eq. (B1) for the elastic shell reduces to

$$\frac{1}{c_s^2}\frac{\partial^2 u_r}{\partial t^2}=\frac{\partial}{\partial r}\frac{1}{r^2}\frac{\partial}{\partial r}r^2u_r, \tag{B2}$$

with c_s the longitudinal speed of sound in the shell

$$c_s=\sqrt{\frac{E(1-\nu)}{\rho_s(1+\nu)(1-2\nu)}}. \tag{B3}$$

The fluid velocity $\mathbf{v}(\mathbf{r},t)$ inside the shell is described by the equation of motion for an inviscid fluid (e.g., Ref. [59]),

$$\rho_f\frac{\partial\mathbf{v}}{\partial t}+\rho_f\mathbf{v}\cdot\boldsymbol{\nabla}\mathbf{v}=-\boldsymbol{\nabla}p, \tag{B4}$$

with ρ_f the fluid density and p its pressure. For $\mathbf{v}(\mathbf{r},t)=v_r(r,t)\hat{\mathbf{r}}$, and consequently $p=p(r,t)$ this reduces to

$$\rho_f\frac{\partial v_r}{\partial t}+\frac{1}{2}\rho_f\frac{\partial v_r^2}{\partial r}=-\frac{\partial p}{\partial r}. \tag{B5}$$

If we assume small amplitude oscillations, we can neglect the quadratic term in v_r, leaving

$$\rho_f\frac{\partial v_r}{\partial t}=-\frac{\partial p}{\partial r}. \tag{B6}$$

Furthermore, as long as the compression is small (as is the case for small amplitude oscillations)

$$\partial p/\partial t=-\kappa\boldsymbol{\nabla}\cdot\mathbf{v}=-\kappa\frac{1}{r^2}\frac{\partial}{\partial r}r^2v_r, \tag{B7}$$

with κ the bulk modulus. Differentiating both sides of Eq. (B7) with respect to time and using Eq. (B6), we then arrive at

$$\frac{1}{c_f^2}\frac{\partial^2 p}{\partial t^2}=\frac{1}{r^2}\frac{\partial}{\partial r}r^2\frac{\partial p}{\partial r} \tag{B8}$$

which is an equation for undamped, longitudinal compressional waves, with $c_f=\sqrt{\kappa/\rho_f}$ the speed of sound in the fluid.

The equations of motion can be solved by seeking solutions of harmonic waves, i.e., by assuming

$$u_r(r,t)=U(r)e^{i\omega t},\quad v_r(r,t)=V(r)e^{i\omega t},\quad p(r,t)=P(r)e^{i\omega t}. \tag{B9}$$

Equations (B2) and (B8) then reduce to

$$\frac{d}{dr}\frac{1}{r^2}\frac{d}{dr}r^2U+\frac{\omega^2}{c_s^2}U=0, \tag{B10}$$

$$\frac{1}{r^2}\frac{d}{dr}r^2\frac{dP}{dr}+\frac{\omega^2}{c_f^2}P=0, \tag{B11}$$

with the general solutions

$$U(r)=Aj_1(\omega r/c_s)+By_1(\omega r/c_s), \tag{B12}$$

$$P(r)=Cj_0(\omega r/c_f)+Dy_0(\omega r/c_f). \tag{B13}$$

Here, $j_n(x)$ and $y_n(x)$ are the nth order spherical Bessel functions of the first and second kind, and the coefficients A,B,C, and D are integration constants, that have to be obtained from the appropriate boundary conditions at the inner and outer surface of the shell.

For small deformations, the stress tensor σ in the shell is related to the displacement vector $\mathbf{u}(\mathbf{r},t)$ according to (e.g., [58])

$$\sigma=\mu(\boldsymbol{\nabla}\mathbf{u}+\boldsymbol{\nabla}\mathbf{u}^{\dagger})+\lambda\boldsymbol{\nabla}\cdot\mathbf{u}\mathbf{I}, \tag{B14}$$

with $\mathbf{I}$ the unit tensor and μ and λ the Lamé coefficients

$$\mu=\frac{E}{2(1+\nu)},\quad \lambda=\frac{E\nu}{(1+\nu)(1-2\nu)}. \tag{B15}$$

Using spherical symmetry, $\mathbf{u}(\mathbf{r},t)=u_r(r,t)\hat{\mathbf{r}}$, this gives

$$\sigma_{rr}=(\lambda+2\mu)\frac{\partial u_r}{\partial r}+2\lambda\frac{u_r}{r}. \tag{B16}$$

Balancing the radial stress with the pressure at the inner and outer surface of the shell gives $\sigma_{rr}(r,t)=-p(r,t)$ for $r=a$ and $r=b$. Hence, the boundary conditions for the stress are

$$(\lambda+2\mu)\frac{dU}{dr}\bigg|_r+2\lambda\frac{U(r)}{r}=-P(r),\quad r=a,r=b. \tag{B17}$$

These equations are sufficient to solve for the displacement vector of an elastic shell *in vacuo* [in which case $P(a)=P(b)=0$].

For the fluid filled shell we need two more boundary conditions. The first is obtained by requiring the pressure to be finite at $r=0$, giving $D=0$. The second is obtained by requiring continuity of the normal velocity across the inner surface of the shell, i.e.,

$$v_r(b,t)=\frac{\partial u_r}{\partial t}\bigg|_{r=b}. \tag{B18}$$

Using Eqs. (B6), (B7), and (B9), this reduces to

$$U(b)=\frac{1}{\rho_f\omega^2}\frac{dP}{dr}\bigg|_{r=b}. \tag{B19}$$

1. An elastic shell *in vacuo*

First, we solve for the breathing mode oscillations in an elastic shell *in vacuo*. Substituting Eq. (B12) in Eq. (B17) and using $P(a)=0$ gives

$$A\left[s\alpha j_0(\alpha)-j_1(\alpha)\right]+B\left[s\alpha y_0(\alpha)-y_1(\alpha)\right]=0. \tag{B20}$$

Here, $\alpha=\omega a/c_s$, the constant s is defined as

$$s=\frac{\lambda+2\mu}{4\mu}=\frac{1-\nu}{2(1-2\nu)}, \tag{B21}$$

and we used the fact that $df_n(x)/dx=f_{n-1}(x)-(n+1)f_n(x)/x$, with f_n either j_n or y_n. The boundary condition at $r=b$ leads to an similar expression by substituting $\beta=\omega b/c_s$ for α in Eq. (B20). Eliminating A and B then results in

$$\frac{s\alpha y_0(\alpha)-y_1(\alpha)}{s\alpha j_0(\alpha)-j_1(\alpha)}=\frac{s\beta y_0(\beta)-y_1(\beta)}{s\beta j_0(\beta)-j_1(\beta)}, \tag{B22}$$

which can be simplified to [60]

$$\frac{\tan(\Omega\hat{h})}{\Omega\hat{h}}=\frac{1+s\Omega^2\hat{a}\hat{b}}{\Omega^2\hat{a}\hat{b}+(s\Omega^2\hat{a}^2-1)(s\Omega^2\hat{b}^2-1)}. \tag{B23}$$

Here, $\hat{h}=h/R,\hat{a}=a/R,\hat{b}=b/R$, and the dimensionless frequency Ω is defined as

$$\Omega=\frac{\omega R}{c_s}. \tag{B24}$$

Equation (B23) can be solved numerically for Ω. It has a single solution Ω_0 in the limit $\hat{h}\to 0$,

$$\Omega_0=\sqrt{\frac{2(1+\nu)(1-2\nu)}{(1-\nu)^2}}, \tag{B25}$$

which is Lamb's breathing-mode frequency for an infinitely thin elastic shell *in vacuo* [52]. At finite h, there is a hierarchy of solutions; the lowest frequency being a generalization of Lamb's breathing-mode frequency for shells with a finite thickness. The next higher frequency, which is proportional to R/h, is a mode where the shell's middle surface remains stationary in time and the shell itself becomes thinner (compressed) and thicker (expanded) in an oscillatory manner.

2. An elastic shell filled with an inviscid fluid

Next, we solve for the breathing mode oscillations in an elastic shell filled with an inviscid fluid. The general solution is given by Eqs. (B12) and (B13), where A,B, and C have to be obtained from Eqs. (B17) and (B19) (remember that $D=0$). Since, $P(a)=0$, as for the elastic shell *in vacuo*, the first boundary condition is identical to that of the empty shell [Eq. (B20)]. Using $P(b)=Cj_0(\omega b/c_f)$, the second boundary condition is obtained from Eq. (B20) by substituting $\beta=\omega b/c_s$ for α, and changing the right-hand side to $-(b/4\mu)Cj_0(\omega b/c_f)$. With Eqs. (B12) and (B13), and $dj_0(x)/dx=-j_1(x)$, the third boundary condition (B19) reduces to

$$Aj_1(\beta)+By_1(\beta)=-\frac{C}{\omega\rho_f c_f}j_1\left(\frac{\omega b}{c_f}\right). \tag{B26}$$

Eliminating A,B, and C and simplifying the result using the same notation as in Eq. (B23) gives

$$\begin{aligned}\left[\Omega^2\hat{a}\hat{b}+(s\Omega^2\hat{a}^2-1)(s\Omega^2\hat{b}^2-1)\right]\tan(\Omega\hat{h})-\left(1+s\Omega^2\hat{a}\hat{b}\right)\Omega\hat{h}\\ =\frac{s\Omega\hat{b}}{\gamma f}\frac{j_0(\gamma\Omega\hat{b})}{j_1(\gamma\Omega\hat{b})}\Big[(s\Omega^2\hat{a}^2-\Omega^2\hat{a}\hat{b}-1)\tan(\Omega\hat{h})+\Omega\hat{h}\\ +s\Omega^3\hat{a}^2\hat{b}\Big],\end{aligned} \tag{B27}$$

which can be solved numerically for given values of R,h,ν, and

$$\gamma=\frac{c_s}{c_f},\quad f=\frac{\rho_s}{\rho_f}. \tag{B28}$$

Expanding Eq. (B27) in powers of h and keeping only the lowest order gives

$$\left[1-\frac{\rho_f R}{\rho_s h}\frac{j_0(\gamma\Omega)}{\gamma\Omega j_1(\gamma\Omega)}\right]\left(\frac{\Omega}{\Omega_0}\right)^2=1, \tag{B29}$$

with Ω_0 given in Eq. (B25). This result is identical to that obtained by Rand and DiMaggio [61] and Engin and Liu [62] for $n=0$, and reduces to that obtained from membrane theory for $\nu=1/2$ [63]. Note that for $\rho_f/\rho_s \to 0$, Eq. (B29) reduces to $\Omega=\Omega_0$, the correct result for an infinitely thin elastic shell *in vacuo*. For $\gamma \to \infty$, with c_f finite, it degenerates to

$$j_1\left(\frac{\omega b}{c_f}\right)=0, \tag{B30}$$

which is the frequency equation for radial oscillations of an inviscid fluid inside a rigid spherical cavity with radius b. The same result could have been obtained directly, by solving Eq. (B11), subject to the boundary condition (B19) for $U(b)=0$.

[1] K. Perktold and G. Rappitsch, J. Biomech. **28**, 845 (1995).
[2] J. B. Grotberg and O. E. Jensen, Annu. Rev. Fluid Mech. **36**, 121 (2004).
[3] R. H. Scanlan and R. Rosenbaum, *Introduction to the Study of Aircraft Vibration and Flutter* (The MacMillan Company, New York, 1951).
[4] *Bridge Aerodynamics*, edited by A. Larsen and S. Esdahl (Balkema, Rotterdam, 1998).
[5] M. P. Rast, Int. J. Numer. Methods Fluids **19**, 1115 (1994).
[6] J. M. T. Penrose and C. J. Staples, Int. J. Numer. Methods Fluids **40**, 467 (2002).
[7] P. R. F. Teixeira and A. M. Awruch, Comput. Fluids **34**, 249 (2005), and references therein.
[8] A. A. Gusev, Phys. Rev. Lett. **93**, 034302 (2004).
[9] S. Chen and G. D. Doolen, Annu. Rev. Fluid Mech. **30**, 329 (1998).
[10] W. T. Ashurst and W. G. Hoover, Phys. Rev. B **14**, 1465 (1976).
[11] G. A. Buxton, C. M. Care, and D. J. Cleaver, Modell. Simul. Mater. Sci. Eng. **9**, 485 (2001).
[12] T. Kato, K. Sato, R. Sasaki, H. Kakinuma, and M. Moriyama, Cancer Chemother. Pharmacol. **37**, 289 (1996).
[13] N. Elsner, F. Dubreuil, and A. Fery, Phys. Rev. E **69**, 031802 (2004).
[14] G. S. O'Brien and C. J. Bean, J. Geophys. Res. **109**, B09301 (2004).
[15] X. Shan and H. Chen, Phys. Rev. E **47**, 1815 (1993).
[16] M. R. Swift, W. R. Osborn, and J. M. Yeomans, Phys. Rev. Lett. **75**, 830 (1995).
[17] L.-S. Luo and S. S. Girimaji, Phys. Rev. E **66**, 035301(F) (2002).
[18] A. Lamura, G. Gonnella, and J. M. Yeomans, Europhys. Lett. **45**, 314 (1999).
[19] K. Good, O. Kuksenok, G. A. Buxton, V. V. Ginzburg, and A. C. Balazs, J. Chem. Phys. **121**, 6052 (2004).
[20] M. M. Dupin, I. Halliday, and C. M. Care, J. Phys. A **36**, 8517 (2003).
[21] A. Cancelliere, C. Chang, E. Foti, D. H. Rothman, and S. Succi, Phys. Fluids A **2**, 2085 (1990).
[22] R. Verberg and A. J. C. Ladd, Phys. Rev. E **65**, 056311 (2002).
[23] P. Szymczak and A. J. C. Ladd Geophys. Res. Lett. **31**, L23606 (2004).
[24] M. Krafczyk, M. Cerrolaza, M. Schulz, and E. Rank, J. Biomech. **31**, 453 (1998).
[25] M. Hirabayashi, M. Ohta, D. A. Rufenacht, and B. Chopard, Phys. Rev. E **68**, 021918 (2003).
[26] A. J. C. Ladd, J. Fluid Mech. **271**, 285 (1994); **271**, 311, (1994).
[27] C. K. Aidun, Y. Lu, and E.-J. Ding, J. Fluid Mech. **373**, 287 (1998).
[28] A. J. C. Ladd and R. Verberg, J. Stat. Phys. **104**, 1191 (2001).
[29] R. Verberg and D. L. Koch (unpublished).
[30] H. Xu, R. Verberg, D. L. Koch, and M. Y. Louge (unpublished).
[31] M. Krafczyk, J. Tolke, E. Rank, and M. Sculz, Comput. Struct. **79**, 2031 (2001).
[32] H. Fang, Z. Wang, Z. Lin, and M. Liu, Phys. Rev. E **65**, 051925 (2002).
[33] L. Monette and M. P. Anderson, Modell. Simul. Mater. Sci. Eng. **2**, 53 (1994).
[34] G. A. Buxton and A. C. Balazs, J. Chem. Phys. **117**, 7649 (2002).
[35] G. A. Buxton and A. C. Balazs, Phys. Rev. E **67**, 031802 (2003).
[36] L. Monette and M. P. Anderson, Scr. Metall. Mater. **28**, 1095 (1993).
[37] M. P. Anderson, L. Monette, and G. S. Grest, J. Appl. Phys. **75**, 1155 (1994).
[38] G. A. Buxton and A. C. Balazs, Mol. Simul. **30**, 249 (2004).
[39] U. Frisch, D. d'Humières, B. Hasslacher, P. Lallemand, Y. Pomeau, and J.-P. Rivet, Complex Syst. **1**, 649 (1987).
[40] D. d'Humières, I. Ginzburg, M. Krafczyk, P. Lallemand, and L.-S. Luo, Philos. Trans. R. Soc. London, Ser. A **360**, 437 (2002), and references therein.
[41] X. He and L.-S. Luo, Phys. Rev. E **55**, R6333 (1997); **56**, 6811 (1997).
[42] G. N. Hassold and D. J. Srolovitz, Phys. Rev. B **39**, 9273 (1989).
[43] A. J. C. Ladd, J. H. Kinney, and T. M. Breunig, Phys. Rev. E **55**, 3271 (1997).
[44] A. J. C. Ladd and J. H. Kinney, Physica A **240**, 349 (1997).
[45] L. M. Schwartz, S. Feng, M. F. Thorpe, and P. N. Sen, Phys. Rev. B **32**, 4607 (1985).
[46] S. Arbabi and M. Sahimi, Phys. Rev. B **41**, 772 (1990).
[47] M. Tuckerman, B. J. Berne, and G. J. Martyna, J. Chem. Phys. **97**, 1990 (1992).
[48] N.-Q. Nguyen and A. J. C. Ladd, Phys. Rev. E **66**, 046708 (2002).
[49] M. Bouzidi, M. Firdaouss, and P. Lallemand, Phys. Fluids **13**, 3452 (2001).
[50] An alternative approach to improving the local nonequilibrium stress would be to do a few LBM iterations with "frozen" values for the fluid density and velocity.
[51] I. Ginzburg and D. d'Humières, Phys. Rev. E **68**, 066614

(2003), and references therein.
[52] H. Lamb, Proc. London Math. Soc. **14**, 50 (1882).
[53] In order to obtain the images of the deformed elastic shell, we take information from the LSM lattice and map it onto a spherical shell surface. In particular, we consider an unperturbed shell surface, whose dimensions correspond to the unperturbed LSM lattice. We then map the values for both the nodal displacements and equivalent strain from the original unperturbed LSM lattice to the unperturbed shell surface using a simple weighted averaging technique. The shell surface is then displaced according these weighted displacements (obtained from the LSM lattice) in order to obtain the deformed shell surface. Finally, the shell surface is colored according to the weighted values of the equivalent strain from the LSM lattice.
[54] F. J. Higuera, S. Succi, and R. Benzi, Europhys. Lett. **9**, 345 (1989).
[55] Y. H. Qian, D. d'Humières, and P. Lallemand, Europhys. Lett. **17**, 479 (1992).
[56] H. Chen, S. Chen, and W. H. Matthaeus, Phys. Rev. A **45**, R5339 (1992).
[57] P. Lallemand and L.-S. Luo, Phys. Rev. E **61**, 6546 (2000).
[58] L. D. Landau and E. M. Lifshitz, *Theory of Elasticity* (Pergamon Press, London, 1959).
[59] L. D. Landau and E. M. Lifshitz, *Fluid Mechanics* (Pergamon Press, London, 1959).
[60] A. H. Shah, C. V. Ramkrishnan, and S. K. Datta, J. Appl. Mech. **36**, 440 (1969).
[61] R. Rand and F. DiMaggio, J. Acoust. Soc. Am. **42**, 1278 (1967).
[62] A. E. Engin and Y. K. Liu, J. Biomech. **3**, 11 (1970).
[63] P. M. Morse and H. Feshbach, *Methods of Theoretical Physics* (McGraw-Hill, New York, 1953), Pt.II.